

Nanometer-scale, quantitative composition mappings of InGaN layers from a combination of scanning transmission electron microscopy and energy dispersive x-ray spectroscopy

This article has been downloaded from IOPscience. Please scroll down to see the full text article.

2012 Nanotechnology 23 455707

(<http://iopscience.iop.org/0957-4484/23/45/455707>)

View [the table of contents for this issue](#), or go to the [journal homepage](#) for more

Download details:

IP Address: 194.57.150.74

The article was downloaded on 24/10/2012 at 13:26

Please note that [terms and conditions apply](#).

Nanometer-scale, quantitative composition mappings of InGaN layers from a combination of scanning transmission electron microscopy and energy dispersive x-ray spectroscopy

K Pantzas^{1,2}, G Patriarche³, D Troadec⁴, S Gautier^{2,5}, T Moudakir², S Suresh², L Largeau³, O Mauguin³, P L Voss^{1,2} and A Ougazzaden^{1,2}

¹ Georgia Institute of Technology, GT-Lorraine, 2–3 Rue Marconi, F-57070, Metz, France

² UMI 2958, Georgia Tech-CNRS, 2–3 Rue Marconi, F-57070, Metz, France

³ CNRS-Laboratoire de Photonique et des Nanostructures (LPN), Route de Nozay, F-91460, Marcoussis, France

⁴ CNRS, Institut d'Electronique, de Microélectronique et de Nanotechnologie, UMR 8520, F-59652 Villeneuve Dascq, France

⁵ Laboratoire Matériaux Optiques, Photonique et Systèmes (LMOPS), EA4423, Université Paul Verlaine Metz—Supelec, 2 Rue Edouard Belin, F-57070, Metz, France

E-mail: abdallah.ougazzaden@ece.gatech.edu

Received 6 June 2012, in final form 14 August 2012

Published 22 October 2012

Online at stacks.iop.org/Nano/23/455707

Abstract

Using elastic scattering theory we show that a small set of energy dispersive x-ray spectroscopy (EDX) measurements is sufficient to experimentally evaluate the scattering function of electrons in high-angle annular dark field scanning transmission microscopy (HAADF-STEM). We then demonstrate how to use this function to transform qualitative HAADF-STEM images of InGaN layers into precise, quantitative chemical maps of the indium composition. The maps obtained in this way combine the resolution of HAADF-STEM and the chemical precision of EDX. We illustrate the potential of such chemical maps by using them to investigate nanometer-scale fluctuations in the indium composition and their impact on the growth of epitaxial InGaN layers.

(Some figures may appear in colour only in the online journal)

1. Introduction

Indium gallium nitride (InGaN) is used in commercial light-emitting diodes (LEDs), and lasers [1], and is being actively investigated for use in solar cells [2–8]. It is one of many scientifically and economically important materials [9–11] whose quality can potentially be improved if the material were better understood. Detailed chemical mappings of the alloy composition from transmission electron microscopy (TEM) and scanning transmission microscopy

(STEM) images can be particularly interesting in such studies, providing useful insights into material growth.

While both TEM and high-angle annular dark field scanning transmission microscopy (HAADF-STEM) give qualitative chemical information, precise, quantitative maps cannot be readily obtained. Indeed, only relative intensity variations in TEM and HAADF-STEM reflect variations in composition. The difficulty lies in the fact that these relative intensity variations cannot be quantitatively interpreted directly from the TEM or STEM image [12]. In order to do

that, one needs a means of establishing an absolute scale of composition.

Recently, Rosenauer *et al* [13] implemented a method, originally proposed by LeBeau and Stemmer [14], to obtain quantitative chemical maps from HAADF-STEM by fitting frozen lattice simulations to experimental images. In this paper we report an alternative for obtaining quantitative chemical maps from HAADF-STEM. In our case the STEM intensity variations are quantified experimentally, using a small set of energy dispersive x-ray spectroscopy (EDX) measurements as a chemical calibration of the observed intensity variations. This approach combines the chemical precision of EDX with the spatial resolution of HAADF-STEM, to obtain quantitative chemical mappings that cannot be obtained independently from either technique. It presents two advantages over direct EDX mappings: for the EDX signal to be reliably quantifiable, exposure times of more 60 s are required, making 1024×1024 mappings not only impractical but also subject to error due to small displacements of the sample during the acquisition time; moreover, the resolution of EDX is limited by beam-broadening to, at best, 1–2 nm.

In what follows, we first use elastic scattering theory to show how, within certain limits, the scattering law of electrons in HAADF-STEM can be evaluated experimentally through a small set of EDX measurements. We proceed to describe how to compute this scattering law in practice. Then we demonstrate how to use the resulting function to transform qualitative *Z*-contrast images of InGaN layers into precise, quantitative maps that reflect the variations of indium composition in these layers with nanometer-scale precision. Using the results from such maps we provide useful insights into the impact of fluctuations in the indium composition on the growth of epitaxial InGaN layers.

2. Experiment

The InGaN epilayers used for this study were all grown on commercial gallium nitride (GaN)/sapphire templates by metal–organic vapor-phase epitaxy (MOVPE), using nitrogen as the carrier gas and tri-methyl indium (TMIn), tri-methyl gallium (TMG) and ammonia (NH₃) as precursors for elementary indium, gallium and nitrogen, respectively. The growth temperature was 800 °C. Two samples among them are discussed below. Sample A was 70 nm thick, while sample B was 140 nm thick. The TMIn/III, the ratio of TMIn to the sum of TMIn and TMG, for sample A was 15%, while that of sample B was 25%.

X-ray diffraction (XRD) measurements were performed in a Panalytical X'Pert Pro diffractometer in a triple axis configuration. In order to perform accurate composition and strain measurements, reciprocal space mappings (RSMs) were taken along both the symmetric $(0\ 0\ 0\ 6)$ and asymmetric $(1\ 1\ \bar{2}\ 4)$ reflections. The effect of tilt was taken into account by averaging the results from measurements along all six asymmetric φ reflections of the wurtzite lattice, as suggested by Moram and Vickers [15]. The composition was then obtained by numerically solving the third-order polynomial

linking the composition to the *a* and *c* parameters of wurtzite layers for any strain layers, introduced by Schuster *et al* [16].

Specimens from the samples were then prepared for STEM using focused ion beam (FIB) thinning and ion milling. The specimens were 80 nm thick. In order to preserve the sample surface during FIB preparation, a surface coating consisting of a 50 nm-thick layer of carbon, followed by 100 nm of silicon nitride (Si₃N₄) was applied. Prior to STEM imaging, the specimens were cleaned using an argon plasma cleaner.

STEM and EDX were then performed in an aberration-corrected JEOL 2200FS microscope, operating at 200 kV with a probe current of 150 pA, and a probe size of 0.12 nm at the full width at half maximum (FWHM). The convergence half-angle of the probe was 30 mrad and the detection inner and outer half-angles for the HAADF-STEM images were 100 and 170 mrad, respectively. The samples were imaged along the $(1\ 1\ \bar{2}\ 0)$ zone axis.

Compared to TEM, which is known to cause image artifacts due to electron beam damage [17], currents of at most a few hundred pA are used in STEM and are expected to leave no residual damage on the specimen. Although the stability of InGaN in HAADF-STEM in particular has been demonstrated previously [13], we ensured that this was the case here also by taking several sets of images and comparing them. No change was observed in the sample between the different sets of measurements.

Quantitative measurements of the indium composition from EDX were obtained from the intensity ratio of the $L\alpha$ line of indium (3.290 keV) to the $K\alpha$ line of gallium (9.770 keV). The K line of elementary nitrogen (0.392 keV) was also taken into account and revealed that the alloy is stoichiometric. The acquisition time for each EDX spectrum was 60 s, during which no drift in the position of the electron beam was observed. The EDX spectra were acquired using a JEOL 2300D detector and the accompanying JEOL software. The *k*-factors used by the software had been previously re-calibrated using GaAs, InP, GaN, AlN, GaP and GaSb, as well as the ternary alloys In_{0.48}Al_{0.52}As and In_{0.53}Ga_{0.47}As. These alloys are lattice-matched to InP, allowing the composition to be precisely determined through XRD.

3. Quantification of the *Z*-contrast

In this section we explain how the quantification works. We first give a proof of principle from first-principles calculations. We then proceed to present an algorithm to implement it. Finally, we use the algorithm to quantify a HAADF-STEM image of sample A. This example is used to evaluate the spatial resolution and chemical precision of the algorithm.

3.1. Proof of principle

It has been shown that in HAADF-STEM, at detection inner half-angles greater than 60 mrad and for STEM specimens thinner than 100 nm the major contribution to the collected intensity is that of elastically scattered electrons [18]. In

particular it has been shown that a good approximation of the fraction of the incident electron beam intensity scattered towards those angles by an atomic column of the STEM specimen is given by [19]

$$\mathcal{I}_n \propto d \langle \mathcal{Z} \rangle^\alpha. \quad (1)$$

Here, d is the length of the imaged atomic column (i.e. the STEM specimen thickness), $\langle \mathcal{Z} \rangle$ is its average atomic number and α is an exponent that will be discussed in more detail later.

For an atomic column of $\text{In}_x\text{Ga}_{1-x}\text{N}$ the average atomic number is given by

$$\langle \mathcal{Z} \rangle_{\text{InGaN}} = x\mathcal{Z}_{\text{In}} + (1-x)\mathcal{Z}_{\text{Ga}} + \mathcal{Z}_{\text{N}}, \quad (2)$$

or, equivalently,

$$\langle \mathcal{Z} \rangle_{\text{InGaN}} = x\mathcal{Z}_{\text{InN}} + (1-x)\mathcal{Z}_{\text{GaN}}, \quad (3)$$

where $\mathcal{Z}_{\text{III-N}} = \mathcal{Z}_{\text{III}} + \mathcal{Z}_{\text{N}}$.

Thus, one can relate the root α of \mathcal{I}_n to the concentration x of an atomic column of $\text{In}_x\text{Ga}_{1-x}\text{N}$ by the following equation:

$$\sqrt[\alpha]{\mathcal{I}_n} = \sqrt[\alpha]{Kd}(x\mathcal{Z}_{\text{InN}} + (1-x)\mathcal{Z}_{\text{GaN}}). \quad (4)$$

K is a proportionality coefficient that depends on the imaging geometry and which is constant during the acquisition of the HAADF-STEM image. If one divides both sides of equation (4) by the reference intensity $\mathcal{I}_{\text{ref}} = Kd\mathcal{Z}_{\text{GaN}}^\alpha$, one finds an intensity ratio R that is linked to the composition by

$$\sqrt[\alpha]{R} = (\zeta - 1)x + 1, \quad (5)$$

where $\zeta = \frac{\mathcal{Z}_{\text{InN}}}{\mathcal{Z}_{\text{GaN}}}$ is the ratio between the atomic numbers of pure indium nitride (InN) and pure GaN.

From equation (5) it is obvious that if one were to know the value of α , one could readily invert the equation and find

$$x = \xi(\sqrt[\alpha]{R} - 1), \quad (6)$$

where $\xi = \frac{1}{\zeta - 1}$ is introduced to simplify the notation. Then one could proceed to compute a chemical composition map by applying equation (6) to the HAADF-STEM image.

In elastic scattering theory, the exponent α is equal to 2. However, it has been argued that a more appropriate modeling of Rutherford scattering would need to take into account electron screening. In such cases, α is given by

$$\alpha = 2 - \sigma, \quad (7)$$

where $\sigma \geq 0$ is a factor modeling electron screening. This factor depends both on the scattering atom and the penetration depth of the incident electrons into the atom's electron cloud, which in turn depends on the beam acceleration voltage. As a result, the value of α depends on the material being imaged as well as the imaging conditions. Typical values of α range between 1.7 and 2 [19].

Although one cannot have an *a priori* knowledge of the value of α , one could estimate it using a set of EDX measurements of the composition, $\{x_i\}_{i=1}^M$, measured at the same locations as a set of intensity ratios $\{R_i\}_{i=1}^M$, and then using the following estimator $\hat{\alpha}$:

$$\hat{\alpha} = \left\langle \frac{\log R}{\log((\zeta - 1)x + 1)} \right\rangle_{i=1}^M. \quad (8)$$

In section 3.2 we will discuss an algorithm that computes the estimator $\hat{\alpha}$ and then applies equation (6) to obtain a concentration map.

3.2. Implementation

Here we will discuss how to practically implement the method outlined in section 3.1. The implementation proposed here was carried out in MATLAB, where the HAADF-STEM image is represented by a $N \times N$ matrix, of typical size $N = 1024$. For clarity, we will first introduce a few conventions on notation before giving the details of the implementation.

3.2.1. Notation. As discussed above, each pixel of the STEM image corresponds to an intensity \mathcal{I} collected at position (k, l) of the STEM probe. In what follows, the intensity $\mathcal{I}_{k,l}$, collected at position (k, l) , will be referred to as \mathcal{I} , whereas \mathbf{I} will refer to the matrix of intensities $[\mathcal{I}]_{(k,l)}$. Furthermore, an $N \times N$ matrix of ones will be referred to by $\mathbf{1}_N$.

Point-wise, or element-to-element, matrix division will be denoted by $\cdot ./$, i.e. $\mathbf{C} = \mathbf{A} ./ \mathbf{B}$ will signify:

$$C_{k,l} = A_{k,l}/B_{k,l} \quad \text{for all couples } (k, l) \\ \text{such that } k = 1, \dots, N, \quad l = 1, \dots, N. \quad (9)$$

Finally, a subset of M intensities \mathcal{I}_i , or a set of M EDX measurements x_i will be denoted by $\{\mathcal{I}_i\}_{i=1}^M$ and $\{x_i\}_{i=1}^M$, respectively.

3.2.2. Algorithm. A schematic diagram of the proposed algorithm is given in figure 1. In HAADF-STEM, the intensity is collected by an annular scintillation detector combined with a photomultiplier type (PMT), resulting in the useful signal being added on top of a background intensity from the polarization current of the detector. Thus, the first step consists of measuring the average background signal $\langle \mathcal{I}_b \rangle$ and subtracting it from the collected image intensity matrix \mathbf{I}_{raw} . We then obtain a normalized intensity image \mathbf{I}_n that can be used for the quantification

$$\mathbf{I}_n = \mathbf{I}_{\text{raw}} - \langle \mathcal{I}_b \rangle \cdot \mathbf{1}_N. \quad (10)$$

In the second step, we evaluate the reference intensity I_{ref} defined previously. The reference is taken in the GaN buffer. Since specimen preparation by FIB results in a wedge shaped sample, shown in figure 2, d is a function of the position (k, l) in the image. In practice, one observes an intensity gradient, all the more evident at low magnifications. To account for this, \mathbf{I}_{ref} is obtained through a linear least-squares fit of the GaN part of \mathbf{I}_n , to a first-order, two-dimensional polynomial function. This function is then extrapolated to the whole image, and in particular to InGaN. Since InGaN is not too dissimilar from GaN and the gradient created from FIB is not too pronounced, we expect any residual thickness variations to be significantly smaller than the effect of the wedge.

A point-wise division between the background-free \mathbf{I}_n and the reference intensity $\mathbf{I}_n^{\text{ref}}$ results in the matrix of intensity ratios \mathbf{R} :

$$\mathbf{R} = \mathbf{I}_n \cdot / \mathbf{I}_n^{\text{ref}}. \quad (11)$$

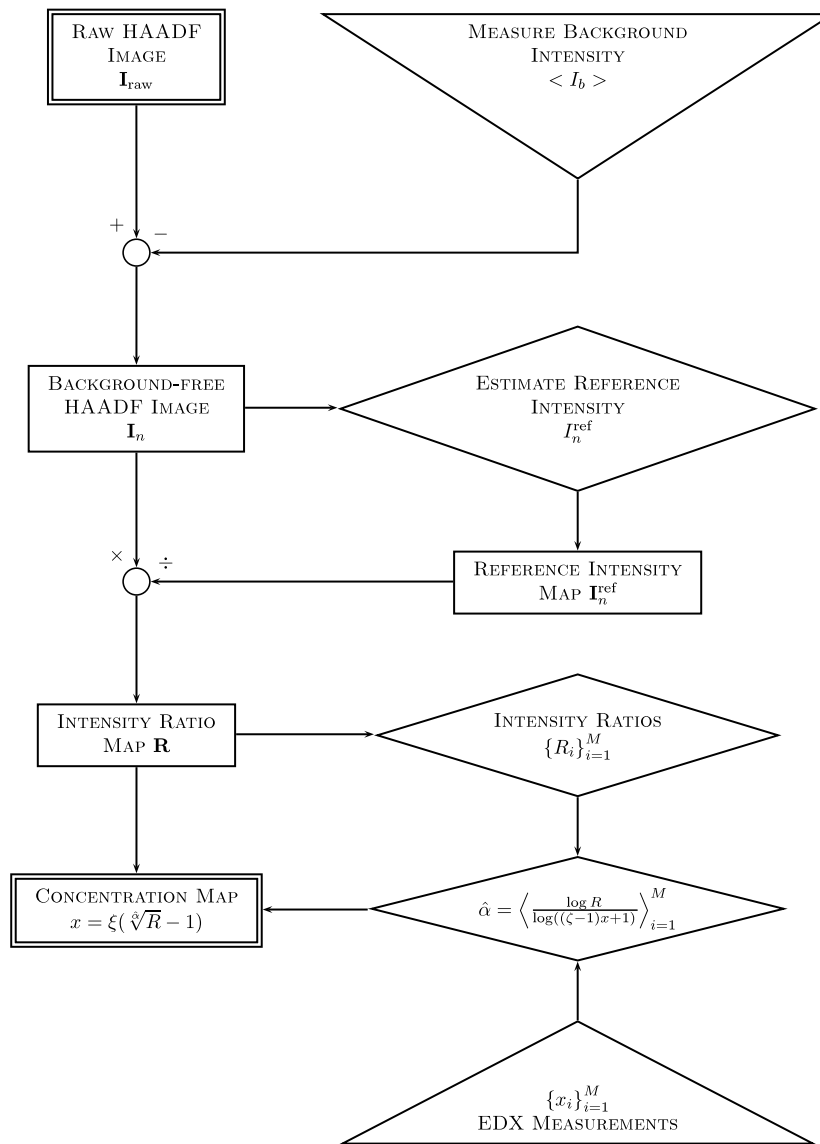


Figure 1. Schematic diagram of the algorithm.

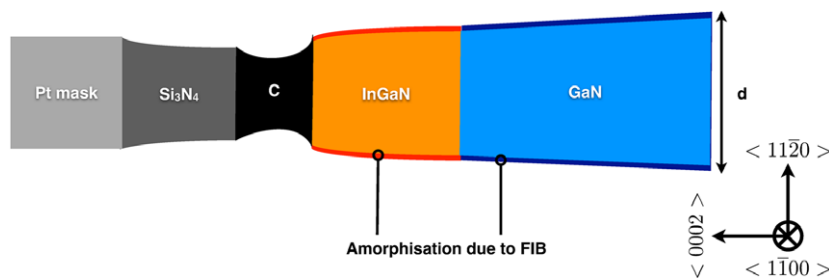


Figure 2. Schematic cross-section of the STEM specimen prepared by FIB. The thickness variation has been exaggerated for visual clarity.

Then, a set $\{R_i, x_i\}_{i=1}^N$ of intensity ratios and the associated composition, independently evaluated by EDX measurements, is used to compute the estimator $\hat{\alpha}$ given by equation (8). Since the EDX probe interacts with a volume of the specimen larger than the STEM probe, it would be inaccurate to use the intensity of the center of the probe as the value R_i used in the estimation. Instead, an average ratio

was computed for each position of the probe, obtained by using a moving average filter on the image. The mask for the moving average filter was obtained by modeling the EDX probe interaction volume by a truncated cone. The diameter was computed as the average between the entry and exit disks. This typically results in a 5×5 matrix for the mask.

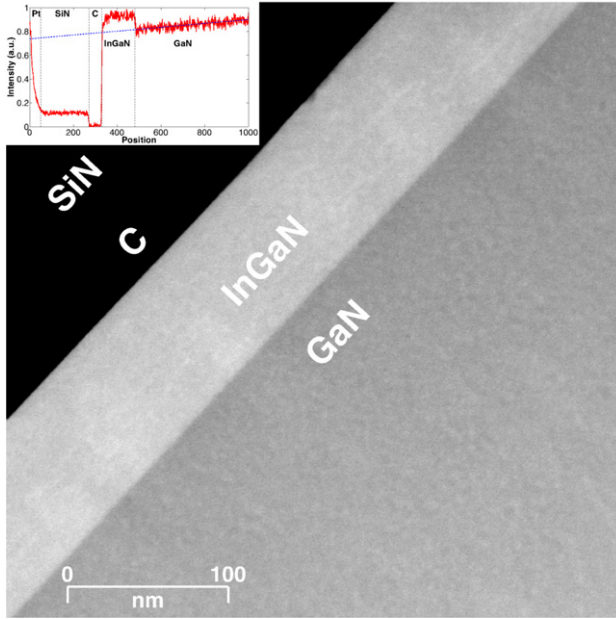


Figure 3. HAADF-STEM image of sample A taken along the $\langle 11\bar{2}0 \rangle$ zone axis. The inset shows the intensity profile from the top left to the bottom right corner of the image. The dashed blue line represents the linearly extrapolated I_{ref} .

Finally, the function given in equation (6), combined with the resulting estimator $\hat{\alpha}$, is applied to the matrix of intensity ratios \mathbf{R} to compute the quantitative composition map.

3.3. Example

In this section we show an example of how the algorithm works on sample A. The spatial resolution and the chemical precision are estimated and limiting factors for both are discussed. Figure 3 shows an HAADF-STEM image of sample A. One clearly distinguishes the GaN template (bottom right), the GaN layer and the carbon–Si₃N₄ cap layer. A close inspection of the GaN layer reveals a slight intensity gradient, roughly perpendicular to the GaN/InGaN interface and towards the bottom right of the image. The gradient becomes evident if one extracts the intensity profile from the top left corner of the image to the bottom right corner, shown in the inset of figure 3. As discussed in section 3.2.2, this gradient can be attributed to the gradient in the sample thickness. The dashed blue line represents the section of the extrapolated I_{ref} along the profile line. It shows that a first-order polynomial is a reasonable approximation of I_{ref} in the area of interest, i.e. the GaN and InGaN layers.

Figure 4 shows an image of the intensity ratio R , obtained in stage three of the algorithm after subtraction of the background intensity and normalization by the reference intensity. The relative intensity variation between GaN and InGaN is preserved, proving that stages 1 and 2 of the algorithm induce no loss of information. A residual modulation of the intensity parallel to the GaN/InGaN interface is still apparent (highlights of the modulation are pointed out by black arrows in figure 4). Profiles taken 10 nm

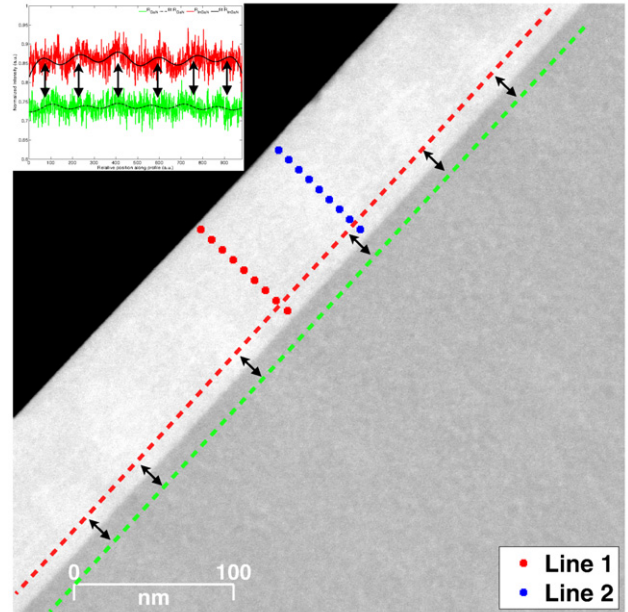


Figure 4. HAADF-STEM image of sample A after subtraction of the background intensity I_B and division by the reference intensity I_{ref} . The inset shows profiles of the intensity ratio R along the dashed red and green lines, respectively. Fits in black are given as a guide to the eye. One can see similar oscillations in the intensity along the two lines, proof of a residual lateral modulation of thickness, associated with the FIB preparation.

on either side of the interface are shown in the inset of figure 4. They reveal that this residual modulation is present in both GaN and InGaN and is related to the FIB preparation of the specimen. The impact of the modulation on the precision of the algorithm will be discussed at the end of this section.

In order to evaluate $\hat{\alpha}$, a set of 18 EDX measurements was performed. The distribution of the EDX measurements across the HAADF-STEM image is shown in figure 4 (red and blue dotted lines). As indicated in section 3.2.2, the corresponding set of intensity ratios $\{R_i\}_{i=1}^M$ was computed by using a moving average filter with a 5 pixel \times 5 pixel mask. This is the required mask size for a 2 nm EDX disk at the magnification used in for the HAADF-STEM image presented in figure 3. It should be noted that this averaging step does not affect resolution of the chemical mappings, since, at this stage, we are estimating the scattering law at places where the composition is known.

Equation (8) was used on the set $\{R_i, x_i\}_{i=1}^M$, shown in table 1. A value of $\alpha = 2 \pm 0.1$ was found to be the appropriate power model in this case. Similar values for the exponent α in the case of InGaN alloys were reported by Amari *et al* [20], using the exact ‘sum-of-squares’ scattering model:

$$R = \frac{xZ_{\text{In}}^\alpha + (1-x)Z_{\text{Ga}}^\alpha + Z_{\text{N}}^\alpha}{Z_{\text{Ga}}^\alpha + Z_{\text{N}}^\alpha}. \quad (12)$$

To check the validity of our approach, we also evaluated the fit of our values to this model. A good fit could not be obtained unless we let $\alpha = 1.7$. This calculation also revealed that, for indium compositions between 0 and 80%, the difference between our model and the sum-of-squares is negligible. Further

Table 1. Summary of the EDX measurements and their corresponding intensity ratios, used for the map presented in figure 5. Numbers in *italic* were excluded from the calculation, since they were located in regions where FIB artifacts were suspected to be present.

	Line 1		Line 2	
	EDX x_i	HAADF R_i	EDX x_i	HAADF R_i
	11.5	1.115	11.4	1.068
	12.9	1.124	<i>13.2</i>	<i>1.121</i>
	12.6	1.140	<i>11.7</i>	<i>1.138</i>
	<i>11.7</i>	<i>1.143</i>	<i>11.9</i>	<i>1.168</i>
	13.8	1.145	<i>12.4</i>	<i>1.168</i>
	14.0	1.110	<i>12.7</i>	<i>1.191</i>
	13.2	1.145	<i>13.0</i>	<i>1.179</i>
	14.5	1.152	<i>12.7</i>	<i>1.168</i>
	<i>12.3</i>	<i>1.109</i>	<i>13.4</i>	<i>1.196</i>
Average	12.9	1.131	12.5	1.155
Standard deviation	1.0	0.017	0.7	0.040

investigation using Ga-poor InGaN alloys may help decide which model is more appropriate. For the purpose of the algorithm presented in this paper either model can be used.

Figure 5 shows the concentration map obtained after application of equation (6). The colorbar indicates the computed indium composition. It has been extended below zero, to better show that the estimation error is randomly distributed around 0 in the GaN layer. The root mean square error (RMSE) between the measured and computed values of the composition was around $\pm 0.5\%$, of the order of the chemical precision of EDX. The resolution of the map is that of the original HAADF-STEM image, since every intensity ratio in the original image was transformed using equation (6).

However, when interpreting the calculated composition, one needs to take into account artifacts introduced by small deviations from the planar thickness model used previously to compute I_{ref} . Indeed, one can distinguish two main sources of artifacts, both related to the FIB preparation of the sample: residual large-scale thickness modulations, such as the ones pointed out by the black arrows in figure 4; and uncertainty due to the amorphous layer on the sidewalls of the specimen, created during the FIB etching. This second source of uncertainty induces an error in both the EDX measurement of the composition and a short-length scale error in the thickness model [21]. In what follows, we will attempt to estimate these errors. All errors are given in atomic %.

The short-scale error in thickness can be evaluated in the GaN part of the concentration map. Indeed, it is responsible for the specularity observed both in the HAADF-STEM image in figure 4 and in the concentration map in figure 5. The standard deviation of the concentration evaluated in the GaN part of the concentration map yields an average error of $\pm 0.5\%$. Finally, the error due to large-scale thickness modulations can be evaluated in the composition map figure 5 by estimating the standard deviation of the composition along a line at the same position as the red dashed line of figure 4. The resulting error is computed at $\pm 1\%$.

Thus, any variations in composition that are less than $\pm 1.5\%$ cannot be detected in this case. A similar precision

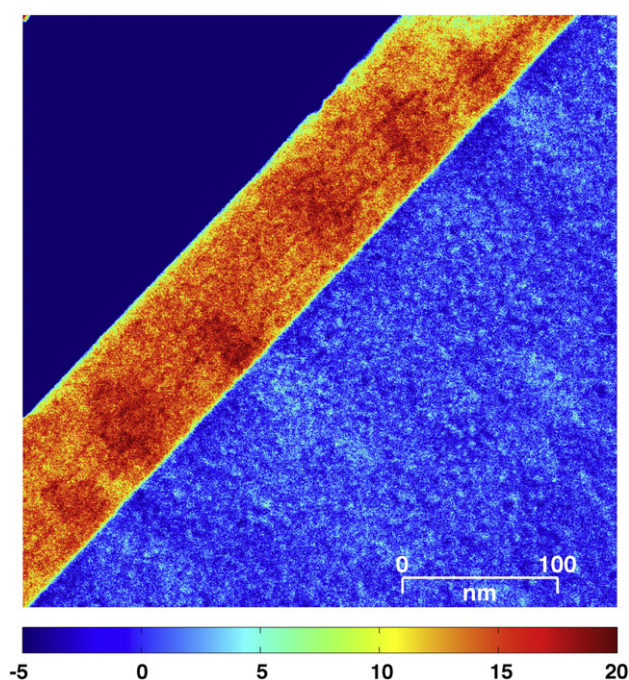


Figure 5. Concentration map of sample A obtained after the application of the algorithm; the colorbar indicates the calculated indium concentration in per cent.

was reported by Rosenauer *et al* in [13]. Further improving the sample preparation may contribute to removing these artifacts and increasing the precision of the map. For the purpose of the application presented in section 4, however, this value was sufficient.

Finally, the results obtained by the algorithm were compared to the concentration deduced from XRD RSMs. Figure 6 shows an average, tilt-free RSM for the asymmetric $\langle 1\ 1\ \bar{2}\ 4 \rangle$ (left) and the symmetric $\langle 0\ 0\ 0\ 6 \rangle$ (right) reflection, respectively. Table 2 compares the indium concentration deduced from XRD, EDX and the concentration map. It shows that the algorithm achieves similar results to what can be found by other techniques. Thus, the chemical mappings obtained can be used reliably in the analysis of InGaN layers.

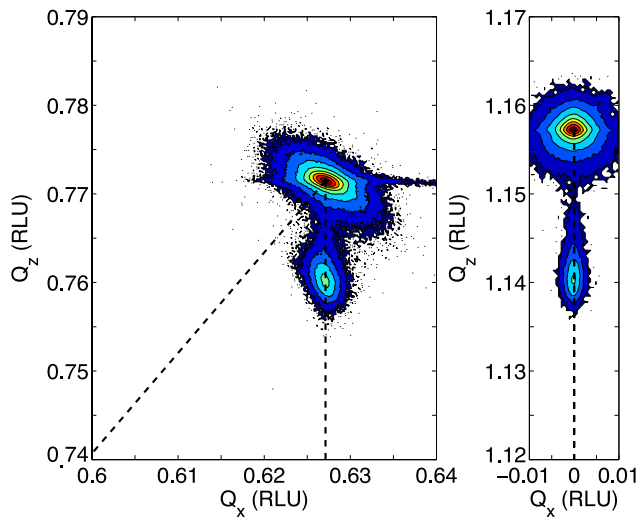
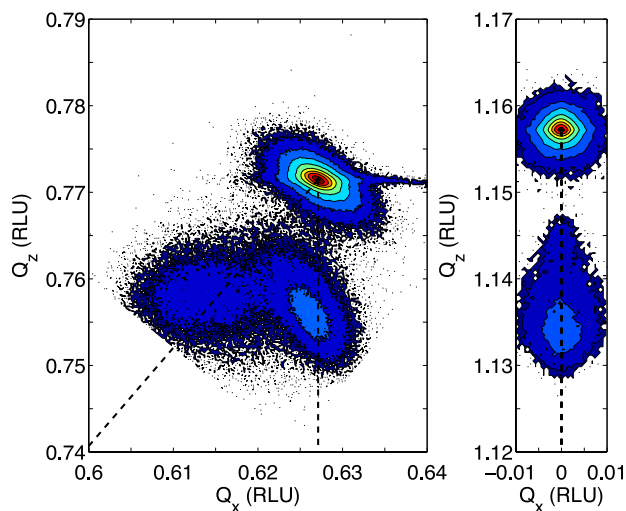
4. Application to InGaN layers presenting double XRD diffraction peaks

In this section, the algorithm is applied to the study of thick InGaN layers presenting double diffraction peaks in XRD RSMs. Sample B is an example of such a case, where two InGaN diffraction peaks besides the intense GaN peak are apparent in both the asymmetric and the symmetric RSM (cf figure 7). The first diffraction spot corresponds to pseudomorphically strained 13% InGaN. This diffraction spot elongates towards its fully relaxed position, indicating an elastic relaxation of strain. The second diffraction spot corresponds to a fully relaxed 20% InGaN layer. Similar results have been observed for thick InGaN layers in [22–29].

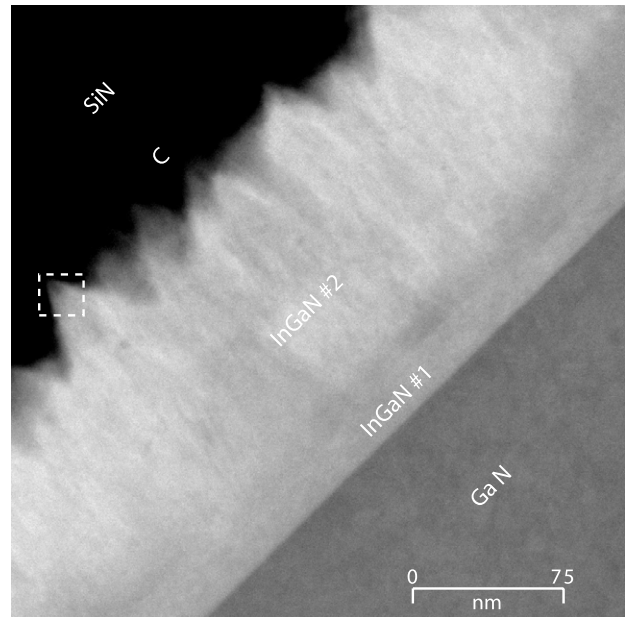
A HAADF-STEM image along the $\langle 1\ 1\ \bar{2}\ 0 \rangle$ zone axis of sample B is shown in figure 8. It is similar to what has been reported in [26–28]. The GaN, InGaN and C/Si₃N₄ cap

Table 2. Average indium composition and the associated standard deviation for both samples, for three different techniques.

		XRD		EDX		EQHAADF	
		Average composition %	Standard deviation %	Average composition %	Standard deviation %	Average composition %	Standard deviation %
Sample A		12	1	12.7	0.9	14	1.4
Sample B	InGaN 1	13.5	1	13	1	14	1.4
	InGaN 2	22	5	23	6	23	5

**Figure 6.** XRD reciprocal space mappings of sample A along the asymmetric $(1\ 1\ \bar{2}\ 4)$ (left) and the symmetric $(0\ 0\ 0\ 6)$ reflection (right), respectively.**Figure 7.** XRD reciprocal space mappings of sample B along the asymmetric $(1\ 1\ \bar{2}\ 4)$ (left) and the symmetric $(0\ 0\ 0\ 6)$ reflection (right), respectively.

layers have been labeled. The image shows that the cap layer preserved the rough surface morphology of the InGaN layer and several pyramids are clearly visible all the way to the top. The presence of these pyramids indicates a three-dimensional

**Figure 8.** HAADF image of sample B. One can clearly distinguish two regions in the InGaN layer: one of homogeneous contrast, close to the interface and above it a second region with rapid variations of the contrast. This is similar to what was observed in [26–28]. The white rectangle gives the location of the images presented in figures 10(a) and (b).

(3D) growth mode, in agreement with results reported in [24, 28, 29].

If one inspects the InGaN layer closely, one can see the presence of two distinct regions: a region of homogeneous contrast near the GaN/InGaN interface, labeled InGaN 1, and a second region, where the contrast fluctuates laterally, concentrated at the top of the InGaN layer, labeled InGaN 2. There are two types of fluctuations in InGaN 2: short-scale variations, of the order of a few nanometers, which give InGaN 2 a ‘veined’ aspect, and long-scale fluctuations, of the order of a few tens of nanometers, concentrated essentially near the interface of the two InGaN sublayers. Figure 9 shows the corresponding chemical composition map. The boundary between InGaN 1 and InGaN 2 is clearly identified in the composition map. The average concentration of InGaN 1 computed by the map is 14%, while that of InGaN 2 is 23%. Thus, InGaN 1 and InGaN 2 can be unambiguously identified as the origin of the fully strained and fully relaxed diffraction spots in the RSM, respectively. It should be noted here that, when computing the average composition of InGaN 2, the

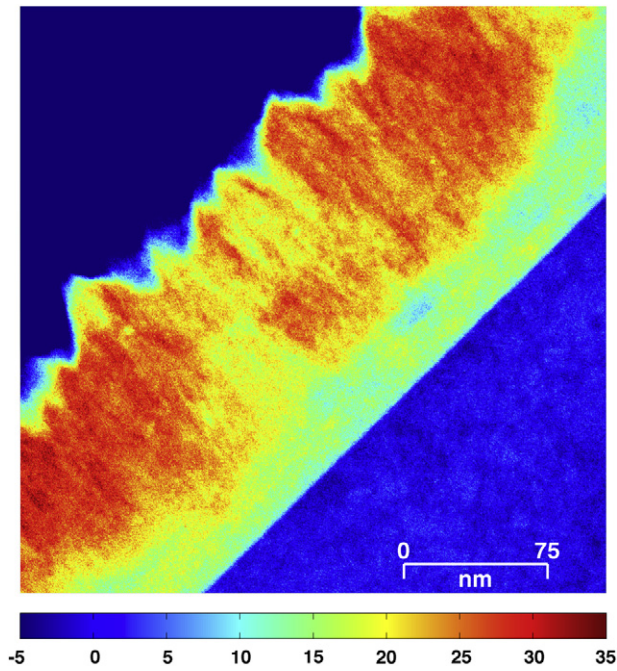


Figure 9. Concentration map obtained of the HAADF presented in figure 8 after the application of the algorithm; the colorbar indicates the calculated indium concentration in per cent.

region within 10 nm of the boundary between InGaN 2 and the carbon layer was excluded. Indeed, due to the pronounced roughness of the InGaN 2 sublayer, there are strong deviations from the first-order thickness model used in the algorithm, which result in erroneous composition estimates.

The map also reveals that both short-scale and long-scale lateral fluctuations in the HAADF intensity in InGaN 2 correspond to variations in the indium concentration of the order $\pm 5\%$. This is significantly higher than the uncertainty due to FIB artifacts and also corresponds to the spread in composition determined using XRD. Due to the rapid variations in the HAADF intensity, it has been argued that the short-scale fluctuations in intensity may be linked to the presence of threading dislocations [27]. In order to check whether the algorithm does not misinterpret these fluctuations, atomic scale resolution images of the pyramids, where the threading dislocations are expected to emerge, were taken to verify if this is the case. An example of the results is given in figure 10(a). It shows an atomic scale resolution HAADF-STEM image of the tip outlined by a white dashed rectangle in figure 8. This particular pyramid was chosen because it is entirely within the FIB section and can be observed all the way to the tip. Moreover, it presents very strong short-scale fluctuations that can be easily misinterpreted. While a line of lower contrast is shown to run through the middle of the pyramid all the way to the top, no disruption of the atomic planes is observed. This is confirmed by the corresponding bright field (BF)-STEM image, shown in figure 10(b). Additional EDX measurements along the dotted red line shown in figure 10(a) (see inset) revealed a local decrease from 22% at the edges of the pyramid to 14% near the middle. We can thus conclude that the map accurately reflects fluctuations of the indium composition.

As discussed in [29], we believe the observed process, i.e. the elastic relaxation of InGaN 1, the transition to 3D growth, the increase in the average indium concentration in InGaN 2 and the lateral fluctuations of indium concentration

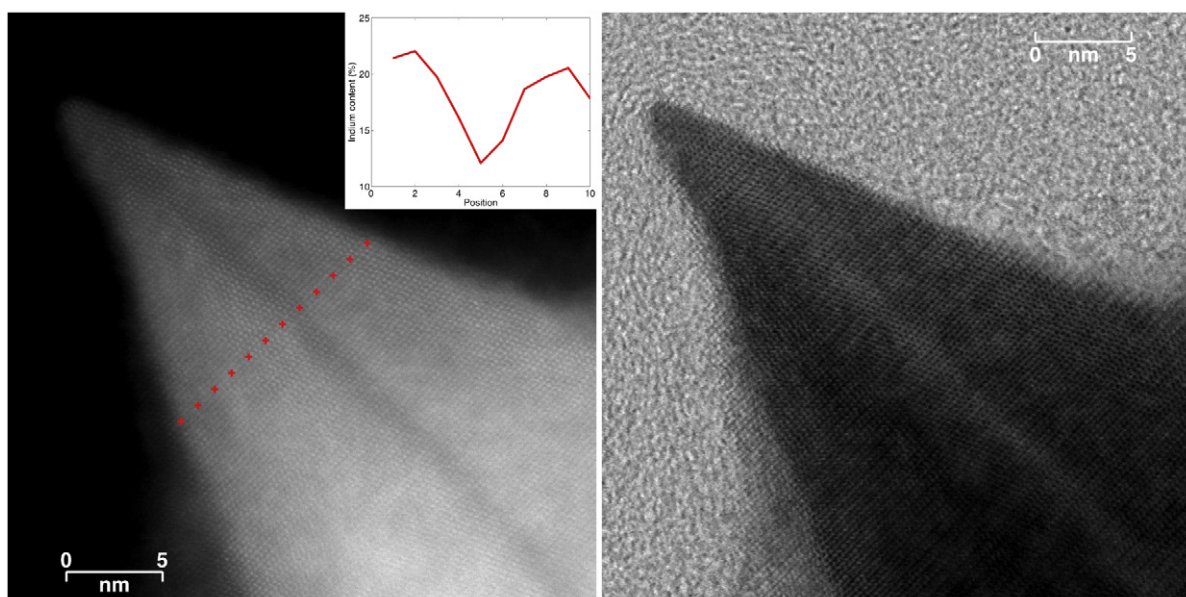


Figure 10. Atomic scale resolution [HAADF (left) and BF (right)] of one of the pyramidal tips. They show no discontinuity in the atomic planes all the way to the top. Thus, the decrease in the HAADF intensity in the middle of the pyramid can only be attributed to a local decrease of the indium concentration in the middle of the pyramid. This is confirmed by EDX measurements (see the inset), revealing a drop in the indium composition along the middle of the pyramid. The red dots indicate the positions of the EDX measurements.

in InGaN 2, to be the result of an accumulation of excess indium at the surface during early stages of growth. This in turn leads to a lateral modulation of the incorporation rate of indium into the lattice, which results in a lateral modulation of the growth rate. This eventually leads to the elastic relaxation of the initial InGaN, the appearance of additional facets favorable to growth and the transition to 3D growth. The strong faceting and eventual 3D growth are evidenced by the roughness of InGaN 2. No particular family of planes is favored in the faceting, as revealed by the presence of pyramids with different basal angles and heights. All pyramids, however, present lateral fluctuations of the composition to some extent. Finally, the stark difference between the average compositions of InGaN 1 and InGaN 2, as well as the significant lateral variations of indium composition in InGaN 2, can be explained by either, or both, of the two following mechanisms:

- (i) The absence of compositional pulling [30, 31] in the elastically relaxed InGaN 2 sublayer.
- (ii) A more favorable binding of indium atoms along the prismatic $\langle 10\bar{1}l \rangle$ planes [32, 33] that make up the facets of the pyramids.

5. Conclusion

In this paper we have shown that it is possible to experimentally evaluate the scattering law of electrons in HAADF-STEM using EDX. In particular, we have evaluated it for InGaN epitaxial layers and used the resulting function to compute quantitative chemical maps of the indium composition. The resulting maps are shown to have nanometric resolution, are precise to 1.5% of the composition and are consistent with results from XRD. Based on these mappings, we have shown that fluctuations in the indium composition are responsible for the spontaneous formation of sublayers with distinct compositions and strain states during the growth of InGaN. Finally, several possible explanations for the origin of these fluctuations are discussed.

Acknowledgment

This study has been funded by the ANR Habisol 2009, project NewPVonGlass.

References

- [1] Nakamura S, Pearton S and Fasol G 2000 *The Blue Laser Diode: The Complete Story (Physics and Astronomy Online Library)* (Berlin: Springer)
- [2] Jani O, Ferguson I, Honsberg C and Kurtz S 2007 *Appl. Phys. Lett.* **91** 132117
- [3] Neufeld C, Toledo N, Cruz S, Iza M, Denbaars S and Mishra U 2008 *Appl. Phys. Lett.* **93** 143502
- [4] Dahal R, Pantha B, Li J, Lin J Y and Jiang H X 2009 *Appl. Phys. Lett.* **94** 063505
- [5] Cai X M, Zeng S W and Zhang B P 2009 *Appl. Phys. Lett.* **95** 173504
- [6] Dahal R, Li J, Aryal K, Lin J Y and Jiang H X 2010 *Appl. Phys. Lett.* **97** 073115
- [7] Matioli E et al 2011 *Appl. Phys. Lett.* **98** 021102
- [8] Lang J, Neufeld C, Hurmi C A, Cruz S, Matioli E, Mishra U and Speck J 2011 *Appl. Phys. Lett.* **98** 131115
- [9] Matsuoka T 2005 *Superlatt. Microstruct.* **37** 19
- [10] Karpov S Y 2011 Modeling of III-nitride light-emitting diodes: progress, problems, and perspectives *Gallium Nitride Materials and Devices VI (San Francisco, CA)* vol 7939, ed J I Chyi, Y Nanishi, H Morkoc, J Piprek and E Yoon
- [11] Hardy M T, Feezell D F, DenBaars S P and Nakamura S 2011 *Mater. Today* **14** 408
- [12] Jinschek J R, Erni R, Gardner N F, Kim A Y and Kisielowski C 2006 *Solid State Commun.* **137** 230
- [13] Rosenauer A et al 2011 *Ultramicroscopy* **111** 1316
- [14] Lebeau J M and Stemmer S 2008 *Ultramicroscopy* **108** 1653–8
- [15] Moram M and Vickers M 2009 *Rep. Prog. Phys.* **72** 036502
- [16] Schuster M, Gervais P, Jobst B, Hosler W, Averbek R, Riechert H, Iberl A and Stommer R 1999 *J. Phys. D: Appl. Phys.* **32** A56
- [17] Humphreys C J 2007 *Phil. Mag.* **87** 1971
- [18] Klenov D O and Stemmer S 2006 *Ultramicroscopy* **106** 889
- [19] Walther T 2006 *J. Microsc.* **221** 137–44
- [20] Amari H, Ross I M, Wang T and Walther T 2012 *Phys. Status Solidi c* **9** 546–9
- [21] Yamazaki T, Watanabe K, Nakanishi N and Hashimoto I 2004 *Ultramicroscopy* **99** 125–35
- [22] Pereira S, Correia M, Pereira E, O'Donnell K, Alves E, Sequeira A, Franco N, Watson I and Deatcher C 2002 *Appl. Phys. Lett.* **80** 3913
- [23] Pereira S, Correia M, Pereira E, Trager-Cowan C, Sweeney F, O'Donnell K, Alves E, Franco N and Sequeira A 2002 *Appl. Phys. Lett.* **81** 1207
- [24] Pereira S 2006 *Thin Solid Films* **515** 164
- [25] de Sousa Pereira S, O'donnell K P and da Costa Alves E 2007 *Adv. Funct. Mater.* **17** 37
- [26] Wang H, Jiang D, Jahn U, Zhu J, Zhao D G, Liu Z, Zhang S and Yang H 2010 *Thin Solid Films* **518** 5028
- [27] Sang L, Takeguchi M, Lee W, Nakayama Y, Lozac'h M, Sekiguchi T and Sumiya M 2010 *APEX* **3** 111004
- [28] Liliental-Weber Z, Yu K M, Hawkrigde M, Bedair S, Berman A E, Emara A, Domagala J and Bak-Misiuk J 2009 *Phys. Status Solidi c* **6** 433
- [29] Pantzas K, Patriarche G, Orsal G, Gautier S, Moudakir T, Abid M, Gorge V, Djebbour Z, Voss P L and Ougazzaden A 2012 *Phys. Status Solidi a* **209** 25
- [30] Pereira S, Correia M R, Pereira E, O'donnell K P, Trager-Cowan C, Sweeney F and Alves E 2001 *Phys. Rev. B* **64** 205311
- [31] Stringfellow G B 2010 *J. Cryst. Growth* **312** 735
- [32] Northrup J E, Romano L T and Neugebauer J 1999 *Appl. Phys. Lett.* **74** 2319
- [33] Wunderer T et al 2008 *Optimization of Semipolar GaInN/GaN blue/green Light Emitting Diode Structures on 1101 GaN side facets (San Jose, CA)* vol 6894, ed H Morkoc, C W Litton, J I Chyi, Y Nanishi and E Yoon p V8490